ELSEVIER

Polymer 43 (2002) 3743–3752

polymer

www.elsevier.com/locate/polymer

# Microscopic damage and macroscopic yield in acrylonitrile–butadiene–styrene (ABS) resins tested under multi-axial stress states

S. Ramaswamy, A.J. Lesser*

*Department of Polymer Science and Engineering, University of Massachusetts, Box 34530, Room 701, Silvio O. Conte Nat. Center for Research, Amherst, MA 01003-4530, USA*

Received 19 November 2001; received in revised form 7 February 2002; accepted 11 February 2002

**Abstract**

In this study, a transparent acrylonitrile–butadiene–styrene polymer alloy was tested in a range of biaxial stress states and a yield locus was generated. The onset of microscopic damage was detected by in situ light transmission measurements. The macroscopic yield locus followed a linear behavior on an octahedral shear stress vs. mean stress plot and the onset of microscopic damage was dependent on both shear and mean stresses. Our findings indicate that macroscopic ductility arises from damage in the polymer at two distinct length scales. On the scale of the rubber particle (0.1–0.2 um), damage occurs via particle debonding from the matrix. At a length scale intermediate between the particle size and macro scale, damage occurs through the formation of micro crack arrays with a well-defined pattern. © 2002 Published by Elsevier Science Ltd.

*Keywords*: Acrylonitrile–butadiene–styrene; Rubber toughening; Damage mechanisms

## 1. Introduction

Polymers are often modified with rubber inclusions to improve their toughness [1–3]. The mechanisms of toughening have been a subject of intense interest and many studies have identified a range of mechanisms that include cavitation [4–11,20,21], crazing [17,24,25], crack bridging [6,7], micro cracking [6,7] and shear banding [4–11]. These mechanisms are operative in the process zone ahead of a crack tip and their sequence together with their relative contribution towards toughness has been a subject of debate. For instance, Pearson and Yee [6] have studied a range of rubber-modified epoxies and have found that cavitation preceded shear yielding of the matrix in systems with smaller rubber particles while others with larger rubber particles exhibited crack bridging. They also conclude that a larger plastic zone results in higher toughness of the material. On the other hand, Huang and Kinloch [12–14] used finite element methods and were able to show that for a given matrix, depending upon the Poisson's ratio and modulus of the rubber, cavitation can occur before or after shear banding. They also contend that cavitation leads to plastic dilatation of the matrix and is independent of shear banding of the matrix.

Lazzeri–Bucknall [5] and Dompas–Groeninckx [20] recently modeled the scale effect in the cavitation resistance of rubber particles. Both models are based on energy balance principles and consider that the energy available to produce cavitation is the volumetric strain energy stored in the rubber particle, $U_0$, given by

$$U_0 = \frac{2}{3}\pi R^3 K_r \varepsilon_v^2 \tag{1}$$

where $R$ is the initial particle radius, $K_r$ is the bulk modulus of the rubber, and $\varepsilon_v = \varepsilon_{ii}$ is volumetric strain. The total energy in the particle after cavitation occurs, $U_C$, is related to the surface energy and cavitation/debond surface area. $U_C$ for the Lazzeri–Bucknall model is given by Eq. (1.1), and for the Dompas–Groeninckx model by Eq. (1.2).

$$U_C = \frac{2}{3}\pi K_r R^3 \left(\varepsilon_v - \frac{r^3}{R^3}\right)^2 + 4\pi r^2 \Gamma + 2\pi r^3 G_r \rho F(\lambda_f) \tag{1.1}$$

$$U_C = 4\pi r^2 \Gamma \tag{1.2}$$

where $r$ is the radius of the cavitated void, $\Gamma$ the surface energy of the rubber, $G_r$ the shear modulus of the rubber, $\rho$ the density ratio of the rubber before and after cavitation, taken equal to 1, and $F(\lambda_f)$ is a numerical integration of the

---

* Corresponding author. Tel.: +1-413-545-0433; fax: +1-413-545-0082.
*E-mail address:* ajl@mail.pse.umass.edu (A.J. Lesser).

PII: S0032-3861(02)00181-7

shear strain function of the rubber after cavitation, taken to be equal to 1.

In both models, the necessary condition for particle cavitation occurs when:

$$U_C \leq U_0. \tag{1.3}$$

For the case of the Dompas–Groeninckx model, the radius of the cavitated surface is calculated by assuming that all of the volume strain in the rubber particle is released upon cavitation (i.e. $r = (\varepsilon_v)^{1/3}R$). The relationship between $r$ and $R$, together with the necessary condition for cavitation (Eq. (1.3)), yields a 'scale effect' for rubber particle cavitation where the larger particles cavitate at lower volume strains than the smaller particles. For the Dompas–Groeninckx model this reduces to:

$$R = \frac{6\Gamma}{K_r \varepsilon_v^{4/3}}. \tag{1.4}$$

Eq. (1.4) defines a critical particle size, $R$, below which cavitation will not occur for a given $\Gamma$, $K_r$ and $\varepsilon_v$. A similar condition can be arrived at using Lazzeri–Bucknall model with the primary difference between the two models being that Lazzeri and Bucknall include the shear energy and residual volumetric energy stored in the rubber particle after cavitation. Both models predict the experimentally observed trend; larger particles cavitate at lower volume strains [26,30]. Eq. (1.4) also means that for a given particle size, there is a critical volumetric strain required for cavitation. For an isotropic elastic material, the critical volume strain is linearly related to a critical hydrostatic or mean stress ($\sigma_{mc}$) through the bulk modulus. The shaded area in Fig. 1 represents a hypothetical condition for rubber particle cavitation in a modified material with a narrow range of particle sizes.

Bucknall [5,21] also proposed that the yield behavior of a cavitated polymeric system could be approximated by a modified Gurson's equation [16], which was originally proposed to describe the effective yield behavior of a porous Von Mises material. Bucknall's equation for the yield locus takes the following form

$$\left(\frac{\tau_y^{oct}}{\tau_{yo}^{oct}}\right)^2 + \mu\frac{\sigma_m}{\tau_{yo}^{oct}}\left(2 - \mu\frac{\sigma_m}{\tau_{yo}^{oct}}\right) + 2(f)\cosh\left(\frac{3\sigma_m}{2\tau_{yo}^{oct}}\right) - f^2 - 1 = 0 \tag{2}$$

where $\tau_y^{oct}$ is the octahedral shear yield stress, $\tau_{yo}^{oct}$ the octahedral shear yield stress in the absence of hydrostatic pressure, $\sigma_m$ the mean stress and $f$ is the volume fraction of cavitated rubber particles. This equation is plotted in Fig. 1 for various values of void fraction $f$. One can consider two trends with respect to Eq. (2): (1) variation of the yield point with $f$ in a given stress state (or equivalently at a prescribed $\tau_{oct}/\sigma_m$) and (2) variation of the yield point with stress state at a given $f$.

1. Crawford and Lesser [19] have reported the yield loci of poly(vinyl chloride) (PVC) modified with methacrylate–butadiene–styrene (MBS) at different concentrations. They found that in pure shear, the octahedral yield stress varied with rubber concentration as
$$\frac{\tau_y^{oct}}{\tau_{yo}^{oct}} = 1 - f. \tag{2.1}$$
It is interesting to note that in the absence of a mean stress ($\sigma_m = 0$), Eq. (2) reduces to a linear function in $f$ as written above. For the PVC systems studied by Crawford and Lesser [19], the effect of stress state and rubber concentration $f$ can be combined and the yield equation can be written as
$$\tau_y^{oct} = \tau_{yo}^{oct}(1 - f) - \mu\sigma_m \tag{2.2}$$
where the value of $\mu$ varied from 0.18 for unmodified PVC to 0.24 for PVC modified with 15% MBS. If $\mu$ is taken as a constant, the above equation for $\tau_y^{oct}$ takes a linear form in $f$ for any given stress state (defined by $\tau^{oct} = A\sigma_m$)
$$\tau_y^{oct} = \tau_{yo}^{oct}\frac{(1 - f)}{(1 + \mu A)}. \tag{2.3}$$
Bucknall's Eq. (2) however does not predict this linear behavior observed for any general biaxial stress state. Also, most other experimental efforts to evaluate the effect of rubber concentration on the macroscopic yield of rubber-modified polymers [4–6,30] have been restricted to only two stress states namely, uniaxial tension and compression.
2. This work examines Eq. (2) over a range of biaxial stress states for a polymer modified with a given concentration of rubber. Transparent acrylonitrile–butadiene–styrene (ABS) is tested in a range of biaxial stress states and the macroscopic yield is determined. The ABS used is initially transparent but becomes opaque (scatters light) when critical conditions were reached, thus allowing for optical verification of microscopic damage in the form of a drop in the intensity of transmitted laser light. From

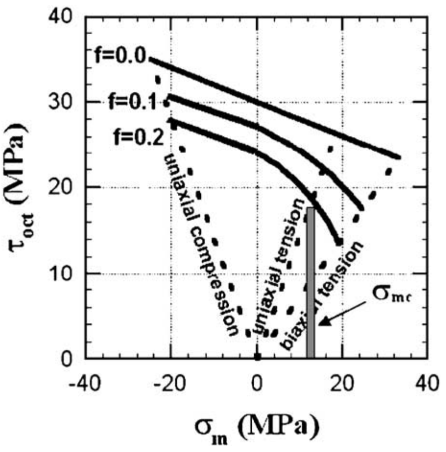

Fig. 1. Yield curve from Eq. (2) and the constant mean stress ($\sigma_{mc}$) criterion for rubber particle cavitation from an energy balance approach (Eq. (1)). $f$ is the volume fraction of cavitated rubber particles. Dotted lines represent different stress states.

these results, the cavitation criterion (constant positive mean stress) from energy balance theories (Eq. (1)) is also evaluated. The damage in different stress states is studied at various length scales using scanning electron microscopy (SEM) and confocal microscopy and the role of the rubber particles together with their relation to different energy absorbing mechanisms is identified.

## 2. Experimental

### 2.1. Material

The transparent ABS (Lustran 266) that was used in this study was in the form of clear pellets provided by Bayer Corporation. The refractive index of the matrix was matched with that of the modifier using a small amount of poly(methyl methacrylate) thus rendering the material transparent.

### 2.2. Specimen fabrication

*Tensile tests*. The ABS was compression molded to 3 mm thick sheets at 220 °C and water cooled to room temperature. The resulting sheets were machined into tensile specimens (ASTM D638 Type I) using a specially designed router.

*Multi-axial tests*. Hollow cylinders of ABS were compression molded using a displacement mold preheated

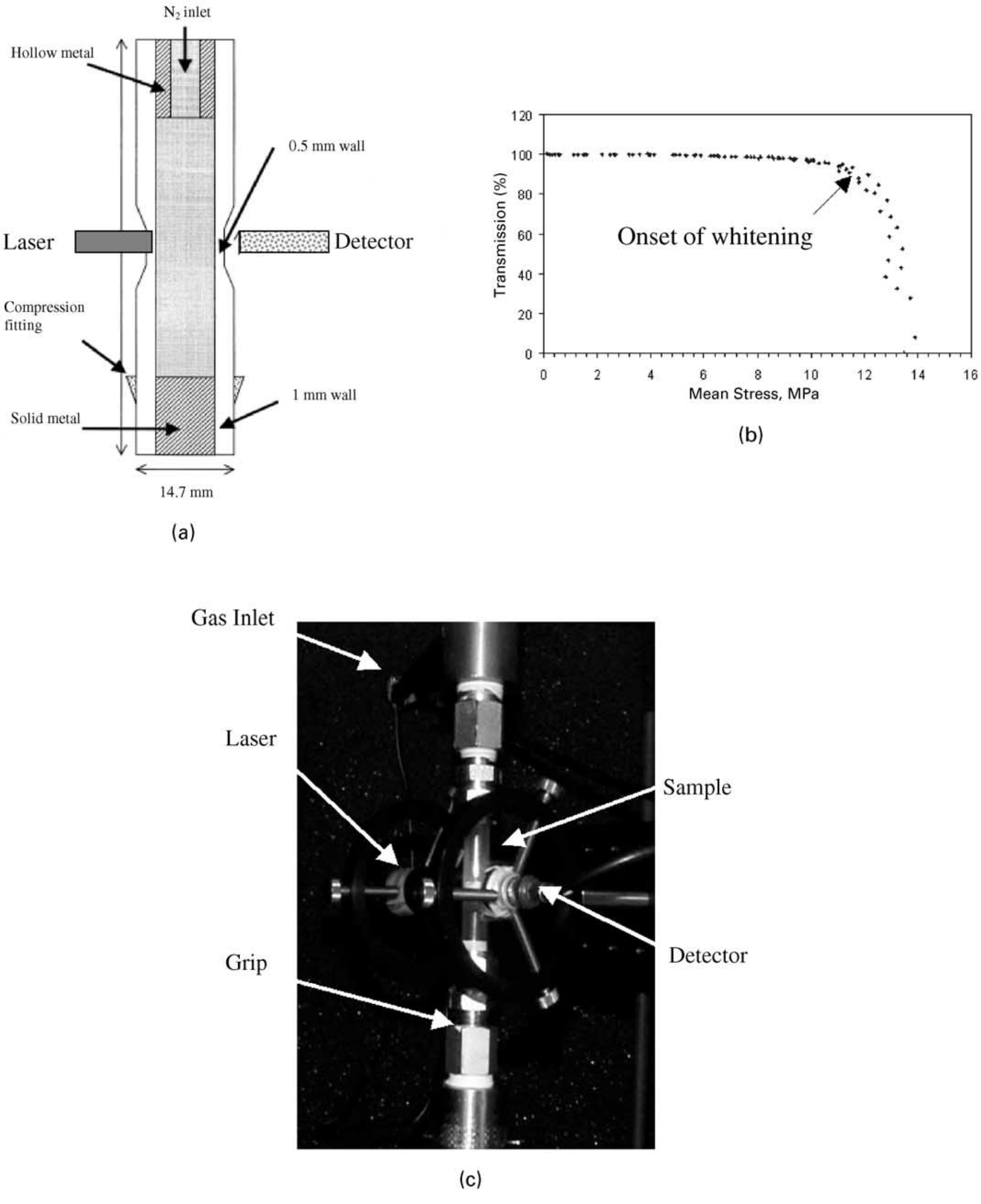

Fig. 2. (a) Sample geometry; (b) transmitted laser intensity vs. stress; (c) test set-up.

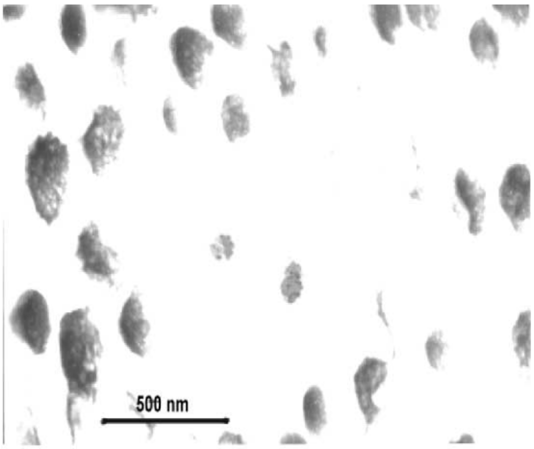

Fig. 3. Rubber particle distribution in ABS.

to 220 °C. The details of biaxial stress states and their control are described later. Twelve grams of polymer was used in one press of the mold, which was left to air cool to room temperature for 2 h (while still under compression). The hollow cylinder was then removed from the mold and machined down in a lathe to create a thinner section as shown in Fig. 2a. This process ensures that the yielding will initiate in the thinner region (higher stresses because of lower cross-sectional area) and provides a location for in situ light transmission measurements (described later). This method of testing has been discussed in detail elsewhere [15,19].

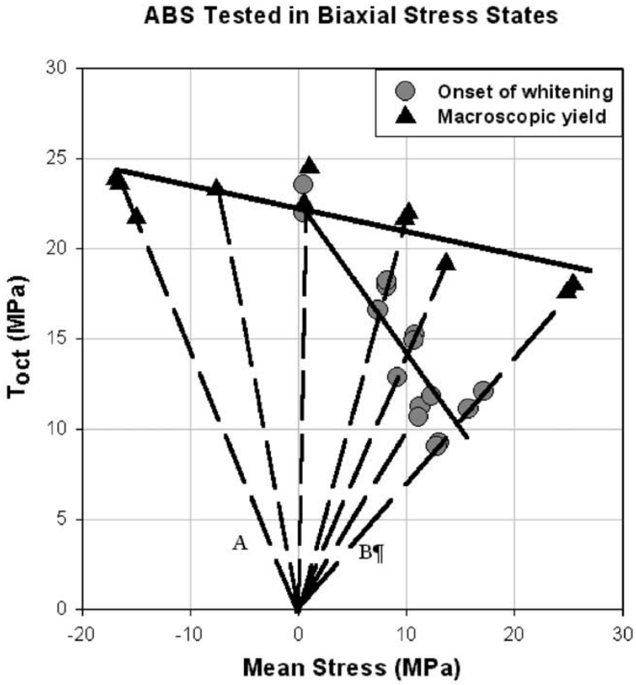

Fig. 4. ABS tested in biaxial stress states. Microscopic and macroscopic behavior.

### 2.3. Tensile tests

Tensile tests were performed at room temperature on an Instron 1123 at a strain rate of $0.021\ \text{min}^{-1}$. This corresponds to an octahedral strain rate of $0.01\ \text{min}^{-1}$, which was used in all the biaxial tests.

### 2.4. Biaxial tests and in situ light transmission measurements

ABS cylinders were tested in different biaxial stress states under pseudo-strain controlled mode using a tension torsion hydraulic Instron modified to apply internal pressure to the hollow cylinder [16,26]. Simultaneous loading and application of internal pressure leads to the following stress state in

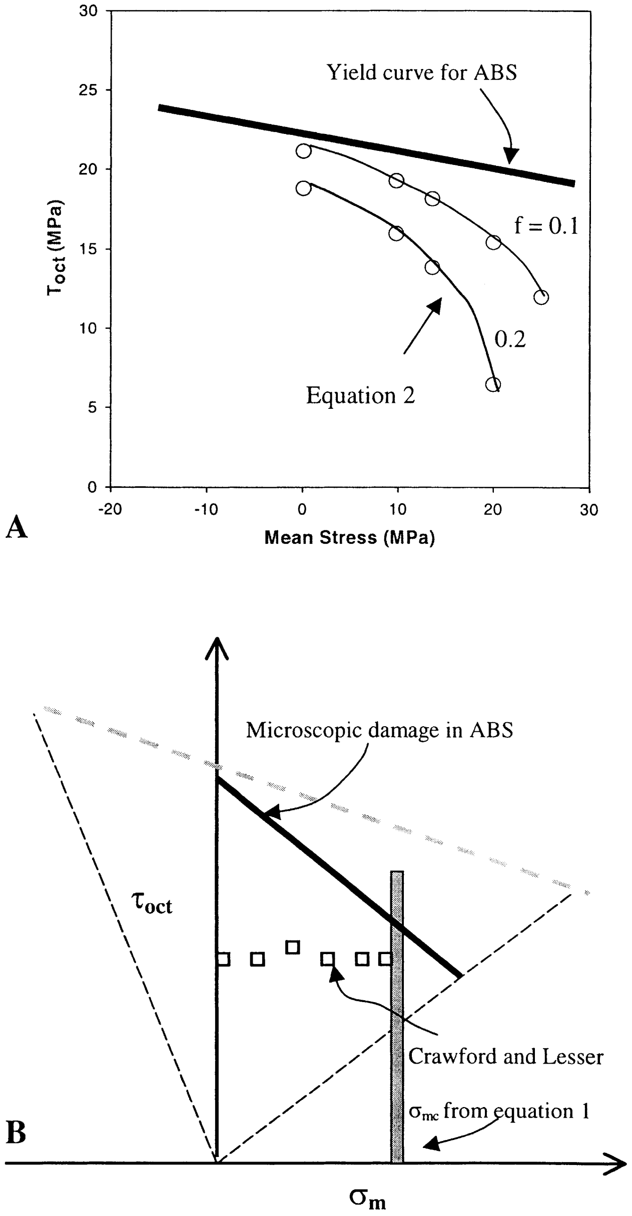

Fig. 5. Comparison of different criteria. (A) Macroscopic yield behavior; (B) microscopic behavior.

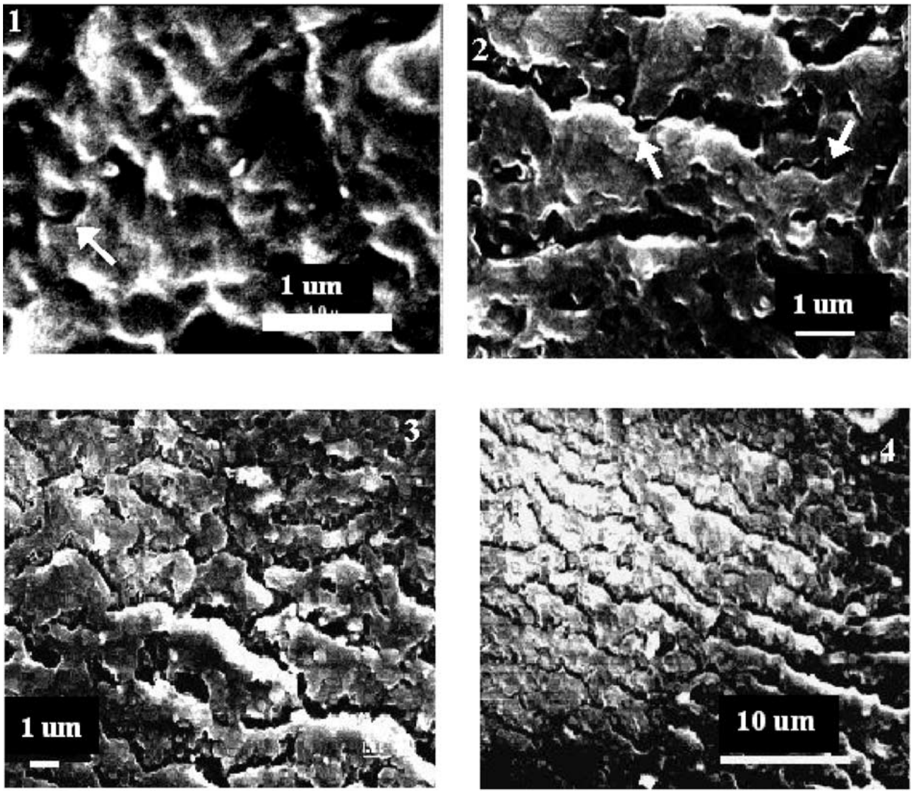

Fig. 6. SEM images showing the different length scales of damage in uniaxial tension. Direction of applied stress is perpendicular to the cracks.

the hollow cylinder:

$$\sigma_1 = \left(\frac{L}{\pi D t}\right) + \left(\frac{pD}{4t}\right), \qquad \sigma_2 = \left(\frac{pD}{2t}\right) \tag{3}$$

where $\sigma_1$ is the axial principal stress, $\sigma_2$ the circumferential principal stress, $L$ the axial load, $p$ the applied internal pressure, $D$ the mean cylinder diameter and $t$ is the wall thickness. Thus by controlling $L$ and $p$, various biaxial stress states can be achieved. The stress in the radial direction is negligible because the thickness of the tube is much smaller compared to its diameter ($D/t \geq 20$).

A laser beam ($\lambda = 633$ nm, beam diameter $= 3$ mm$^2$) was passed through the thinner section of the initially transparent cylinder and the intensity of the transmitted light was detected using a 100 mm$^2$ silicon detector. The transmitted intensity, which remains constant at low levels of stress, drops when critical conditions for cavitation or void formation are reached (Fig. 2b). Thus the onset of microscopic damage was detected using the laser. The experimental set-up is shown in Fig. 2c.

All tests were run at a constant octahedral strain rate of 0.01 min$^{-1}$. Some tests were done to the point of macroscopic yield (defined as a zero slope in the stress versus strain curve) while others were stopped at the onset of whitening (defined as a 10% drop in the intensity of transmitted light). The damage in the samples from the latter tests was analyzed using high resolution SEM, optical and confocal microscopy. The SEM samples were cryo-microtomed and gold coated.

### 2.5. Fracture toughness testing

Three millimeters thick compact tension specimens were loaded to different crack extensions and the corresponding load–displacement ($P$ vs. $\Delta$) curves were obtained. The non-linear energy release rate $J_{1C}$ was calculated from the $J$–$R$ curve generated using the following relationship, details of which have been described by Anderson [28]:

$$J = \frac{\eta}{tb}\int_0^{\Delta} P \, \mathrm{d}\Delta \tag{4}$$

where $t$ is the specimen thickness, $b$ the ligament length, $\Delta$ the displacement, $\eta$ the dimensionless parameter $= 2 + 0.522\, b_0/W$for a compact tension specimen, $b_0$ the initial ligament length, and $W$ is the specimen width.

### 2.6. Analysis of damage

The analysis of damage was done in two length scales: (1) micron level using optical and confocal microscopes, and (2) sub-micron level using a high resolution SEM.

The tested samples were polished along to a smaller thickness on a polishing wheel and then observed under a Bio-Rad MRC-600/1000 confocal microscope operated reflected mode. Voids and cracks present in the sample

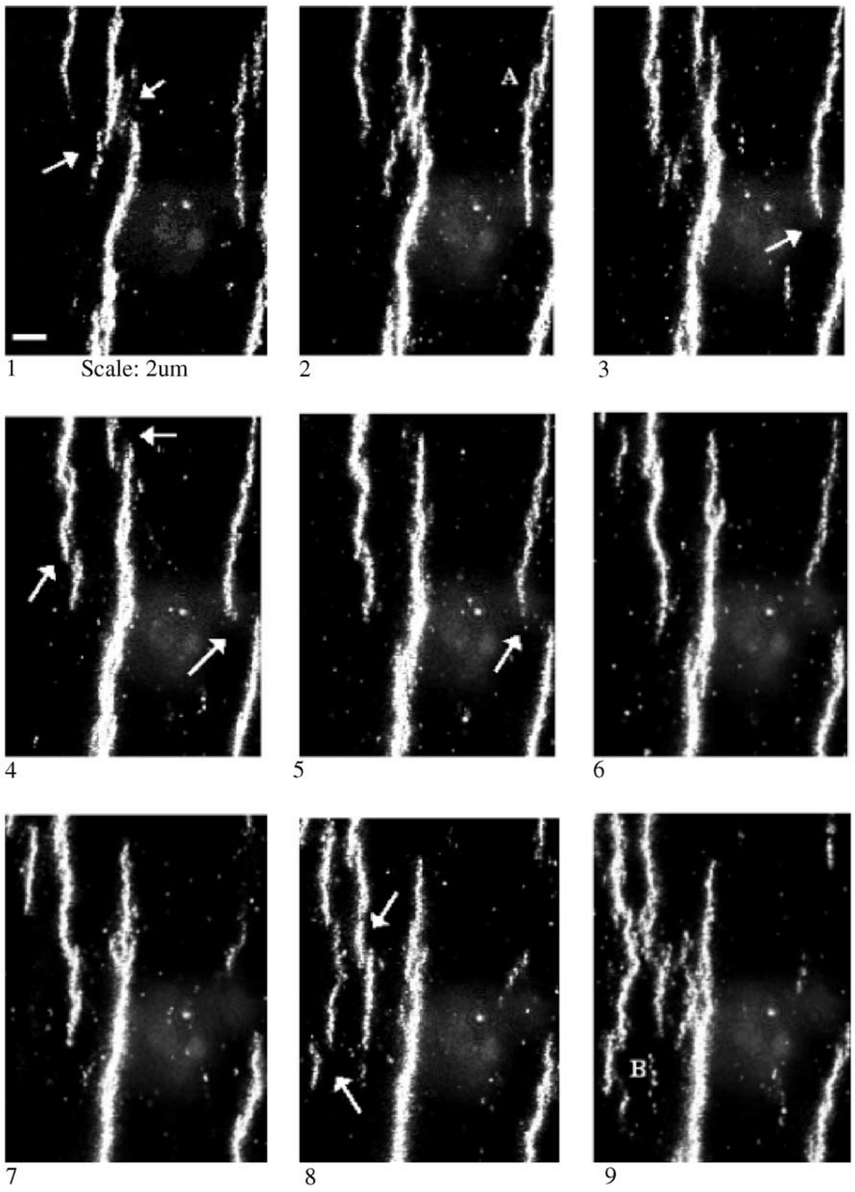

Fig. 7. ABS tested in uniaxial tension. *X–Y* images taken at intervals of 2.7 um in the *z* direction show relative orientation of cracks with depth. Direction of tension is perpendicular to the cracks.

would reflect light and hence appear as bright regions against a dark background in the reflected image. A set of two-dimensional images was obtained at different depths within the sample, which was then manipulated into three-dimensional spatial representation (not reported here). The samples were also studied under a conventional optical microscope.

In order to determine the role of the rubber particles (0.1–0.2 μ size), a high resolution scanning electron microscope (SEM-JEOL JSM-6320 FXV) was used. The damaged samples were embedded in epoxy and cryo-microtomed to make a smooth surface. The surface was then observed using a high resolution SEM operated at 10 kV.

A JEOL 100CX transmission electron microscope (TEM) was used to determine the distribution of butadiene in the styrene–acrylonitrile matrix as shown in Fig. 3.

## 3. Macroscopic yield and microscopic damage in multi-axial stress states

The macroscopic yield behavior and the onset of microscopic damage (or equivalently, the onset of whitening) are shown in Fig. 4. A zero slope of the stress–strain curve in any stress state was taken as the yield point and the onset of whitening was defined as a 10% drop in the intensity of the transmitted laser light.

Two sets of experiments were performed over a range of biaxial stress states ranging from uniaxial compression (A) to equi-biaxial tension (B) (refer to Fig. 4). In one set, hollow cylinders were taken to macroscopic yield and the onset of whitening was recorded. In a second set of experiments, samples were taken to the onset of microscopic

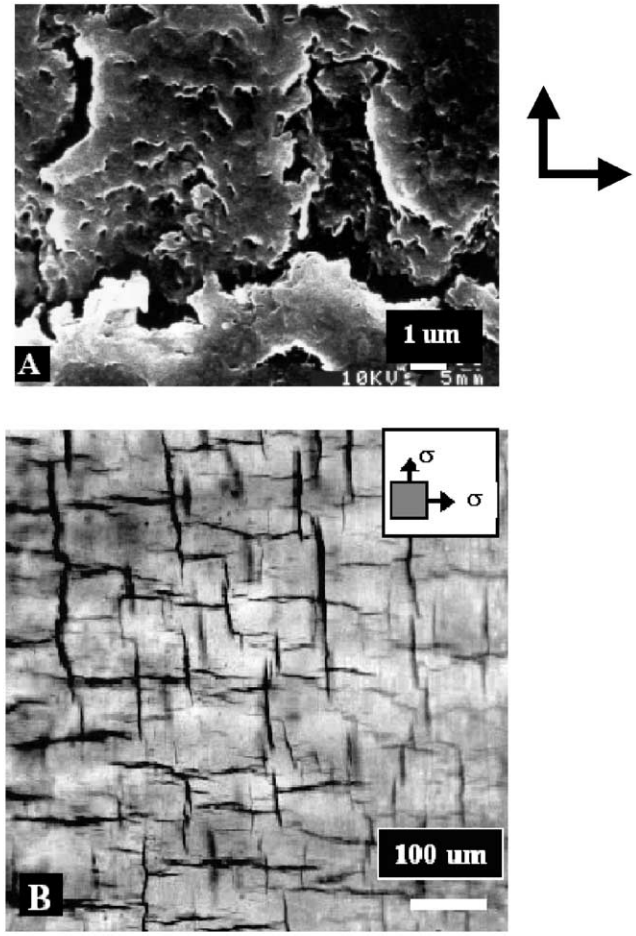

Fig. 8. Damage in equi-biaxial tension. (A) SEM micrograph; (B) optical micrograph.

damage and the testing was stopped. The results of these two sets of experiments are shown together in Fig. 4 in a plot of octahedral shear stress $\tau_{oct}$ vs. mean stress $\sigma_m$.

The first interesting point to note in Fig. 4 is that the macroscopic yield locus is linear in the $\tau_{oct}$ vs. $\sigma_m$ plot. This behavior is characteristic of many polymeric systems and is in accordance with the yield model proposed by Sternstein [27], which is as follows

$$\tau_y^{oct} = \tau_{yo}^{oct} - \mu\sigma_m \tag{5}$$

where the parameters are as defined earlier for Eq. (2). For ABS, $\tau_{yo}^{oct} = 23.5$ MPa and $\mu = 0.11$ which are typical for homogeneous polymers [17–19].

The macroscopically observed yield behavior is compared with Bucknall's yield equation for a precavitated matrix (Eq. (2)) in Fig. 5A. Eq. (2) has been plotted for $f = 0.1$ and $f = 0.2$ with the value of $\mu$ ($\mu = 0.11$) obtained from the slope of the curve in the compressive region ($\sigma_m < 0$) of Fig. 4. In the material tested, $f$ is greater than 0.2. Nevertheless, the mismatch between experimentally observed yield behavior and the predictions of Eq. (2) can be seen clearly. This is not surprising because Eq. (2) was not rigorously derived for pressure dependent materials. Also, the mechanisms of energy absorption after cavitation are different from one of inelastic void growth, an assumption in Eq. (2). These will be discussed in the paragraphs to follow. A linear yield behavior has also been reported for modified PVC systems in Ref. [19].

The microscopic damage in ABS, as indicated by the onset of whitening, also followed Eq. (3) with $\tau_{yo}^{oct} = 23$ MPa and $\mu = 0.89$. This was however valid only in stress states with a positive mean stress. The intensity of the transmitted laser light remained unaltered (no whitening) in stress states where the mean stress was negative. This type of behavior on the microscopic scale is comparable to the constant octahedral shear stress criterion reported by Crawford and Lesser [19] for PVC modified with MBS at different concentrations. However, it is in contrast to the constant positive mean stress criterion obtained by Bucknall [5] and Dompas [20] using energy balance methods (described earlier). The abovementioned criteria are schematically shown together for comparison in Fig. 5B. It is important here to mention that the threshold for the onset of whitening has been set as a 10% drop in the intensity of the initially transmitted light. However, irrespective of this threshold level, interplay between shear and mean stress is observed.

Thus for ABS, our findings differ from the predictions of existing models both at the macroscopic and the microscopic scale. Hence the mechanism of energy dissipation in ABS needs to be investigated.

### 3.1. Mechanisms of damage and energy dissipation

Fig. 6 shows a series of high resolution SEM images that illustrate different length scales of damage in ABS under uniaxial tension. Rubber particles are found to debond from the matrix leading to voids (see arrows in Fig. 6(1,2)) that coalesce to form blunted cracks (Fig. 6(2,3)). These cracks propagate perpendicular to the direction of the applied stress (Fig. 6(4)). Some cracks also bifurcate and deviate locally from the overall direction of propagation (Fig. 6(3,4)). There appears to be a definite spacing associated with this array of cracks (Fig. 6(4)) which effectively softens the material giving rise to a pseudo-ductile response at the macroscopic scale, although brittle failure occurs at the microscopic scale.

The damage in the same stress state but at a larger length scale is shown in Fig. 7, which is a series of confocal microscope images (reflection mode) taken at different depths in the sample. The images explain how the crack configuration changes from that in image 1 (taken at a particular plane say, $P$) to that in image 9 taken about 22 μm below plane $P$. Some cracks (like near A) present in the first few images disappear with depth while other new cracks (like near B) emerge in different locations in the latter images. It can be inferred from these images that the cracks are penny-shaped in three-dimensions and follow one another in space (see

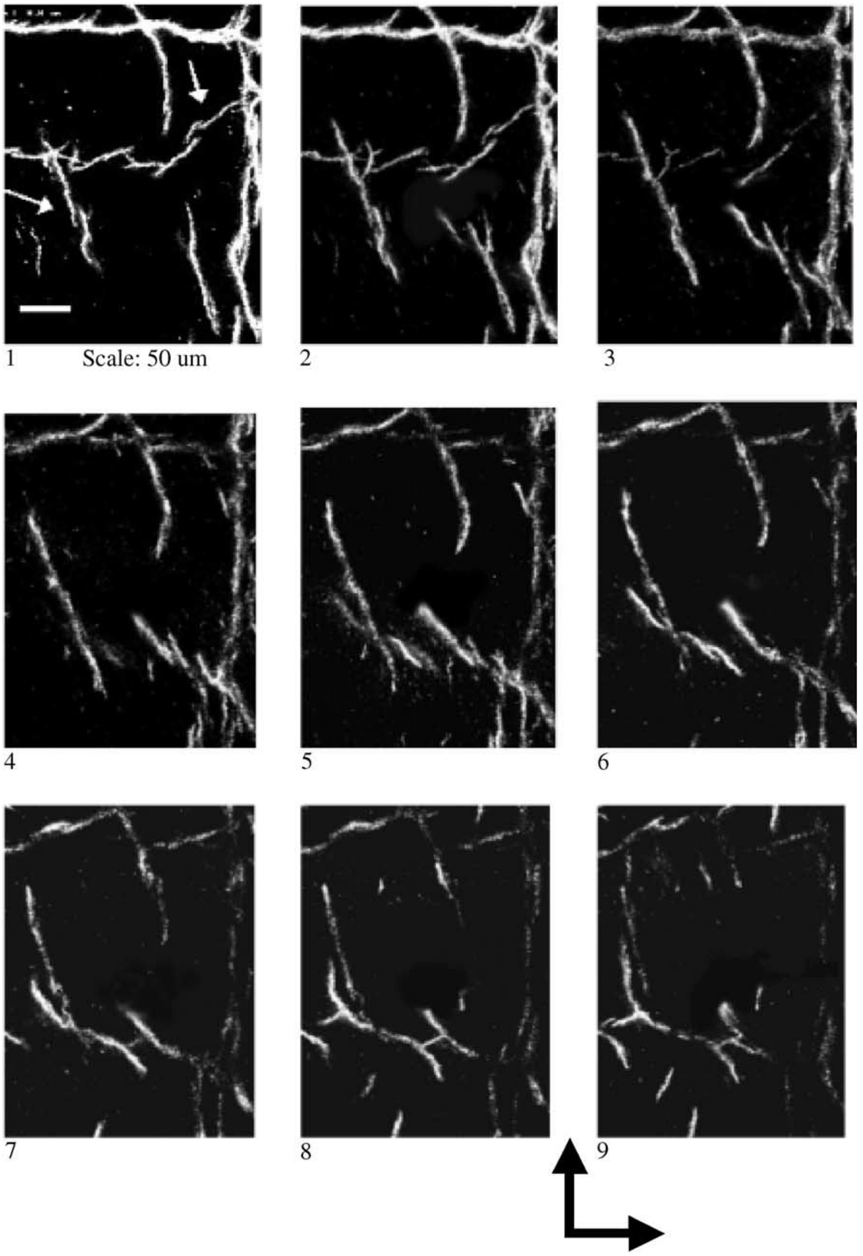

Fig. 9. ABS tested in equi-biaxial tension. $X$–$Y$ images taken at intervals of 9 um in the $z$-direction. Cracks propagate perpendicular to direction of both the principal stresses.

arrows in Fig. 7). We contend that this ‘cascading’ arrangement (one crack trailing another) results in stress reduction at the crack tips (otherwise known as crack shielding), similar to the effect of micro cracking ahead of a main crack [22,23,29]. A parallel array of cracks like in Fig. 6(4) also results in shielding at the crack tips [22,23]. Given the fact that the material fashions its own patterns, they must be energetically favorable.

In equi-biaxial tension, a very interesting crack pattern is observed. Fig. 8B is an optical micrograph of the damage pattern in ABS tested under equi-biaxial tension. Cracks are seen to propagate normal to both the principal directions as if it is a superposition of damage under uniaxial tension applied in mutually perpendicular directions. The crack configuration under equi-biaxial tension can be seen at a higher magnification in the SEM image (Fig. 8A) and also in the confocal microscope images (Fig. 9). However, an isotropic material under truly equi-biaxial loading conditions would create cracks with random orientations. Our observation is a consequence of the fact that in the pseudo-strain controlled mode of testing, the stress state was not strictly equi-biaxial. Nevertheless, the cascading pattern of cracks described earlier replicates itself in both directions. The cracks in the two directions appear to be interacting in an energetically favorable manner.

In any general stress state, the cracks are found to grow

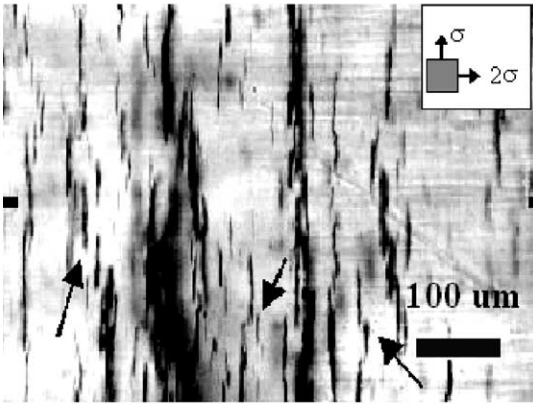

Fig. 10. Optical micrographs of damage in ABS tested in a non-equi-biaxial stress state.

perpendicular to the direction of the maximum tensile principal stress (Fig. 10). Here again, a cascading arrangement of cracks is favored.

It is clear from the above discussion that rubber particle debonding and crack growth leading to an apparent 'shielding-type' of interaction between finite cracks are two mechanisms of energy dissipation in the system. Noting that these are forms of brittle failure, one can anticipate them in the process zone ahead of a propagating crack tip, where the stress state is more triaxial. The plane strain process zone surrounding a crack under Mode I loading is shown in Fig. 11A. The zone extends to almost 4 mm ahead of the crack tip and once again, a network of interacting cracks can be seen (Fig. 11B,C). Crack patterns similar to Figs. 6(4) and 7 can be observed in the process zone. This softens the material in the region ahead of the main crack and is responsible for a large amount of energy dissipation in the system. The $J_{1C}$ calculated was 133.5 KPa m and the tearing modulus was 100.5. The high $J_{1C}$ is commensurate with the large process zone observed.

Note that the size scale of the imposed inhomogeneity in the material is between 0.1 and 0.2 um. The contribution to toughness arises from debonding at the aforementioned length scale and also from crack interaction at a length scale that is an order of magnitude larger that the rubber particles. There also appears to be a self-similarity in the crack pattern at different length scales (see Figs. 7, 10).

## 4. Conclusions

The yield curve for ABS was found to follow a Sternstein type behavior over a range of biaxial stress states. Microscopic damage in the form of voids (arising from debonding of rubber particles) is a function of both shear and mean stresses. These findings are in disagreement with the predictions of existing models (Eqs. (1) and (2)). Furthermore, under positive mean stress, the damage in ABS in any general biaxial stress state is in the form of blunted cracks that propagate perpendicular to the direction of maximum applied tensile principal stress. In equi-biaxial tension, cracks propagate in both the principal directions. These cracks arise due to coalescence of voids formed by debonding of rubber particles from the surrounding matrix material. They appear to be arranged in a manner that might result in mutual stress reduction at the crack tips otherwise known as crack shielding. This could be an energetically favored pattern that self-replicates at different length scales. There seems to be a definite spacing associated with this array of cracks which essentially softens the material giving rise to a pseudo-ductile response at the macroscopic scale although brittle failure occurs at the microscopic scale.

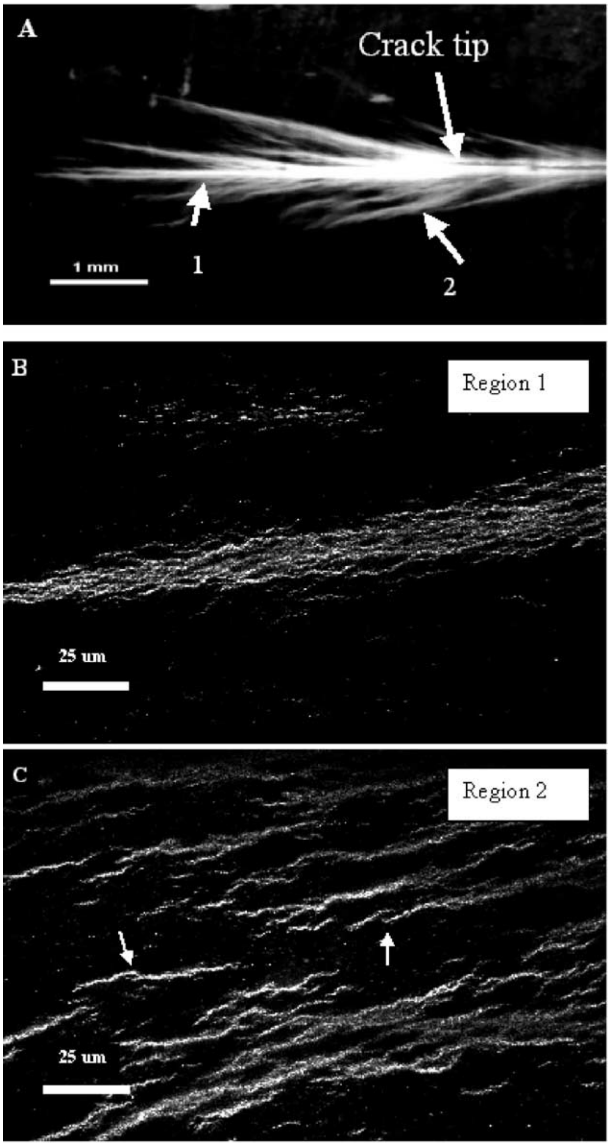

Fig. 11. (A) Plane strain process zone in ABS; (B) crack configuration in region 1; (C) crack configuration in region 2.

## Acknowledgements

We are grateful to Bayer Corporation for their financial support through Cluster C in CUMIRP (Center for UMass & Industry for Research on Polymers). We are also thankful to the reviewers for their comments on our thesis.

## References

[1] Bucknall CB. In: Haward RN, Young RJ, editors. The physics of glassy polymers, 2nd ed. London: Chapman & Hall, 1997. Chapter 8.
[2] Bucknall CB. Toughened plastics. London: Applied Science, 1977.
[3] Kinloch AJ, Young J. Fracture behaviour of polymers. London: Applied Science, 1983.
[4] Bagheri R, Pearson RA. Polymer 1996;37:4529–38.
[5] Lazzeri A, Bucknall CB. J Mater Sci 1993;28:6799.
[6] Pearson RA, Yee AF. J Mater Sci 1991;26:3828–44.
[7] Argon AS, Cohen RE. J Mater Sci 1994;A176:79–90.
[8] Lu F, Cantwell WJ, Kausch HH. J Mater Sci 1997;32:3059.
[9] Parker DS, Sue HJ, Huang J, Yee A. Polymer 1989;31:2267.
[10] Dekkers ME, Hobbs SY, Watkins VH. J Mater Sci 1988;23:1225.
[11] Bensason S, Hiltner A, Baer A. J Appl Polym Sci 1997;63:715.
[12] Huang Y, Kinloch AJ. Polymer 1992:5338.
[13] Huang Y, Kinloch AJ. J Mater Sci Lett 1992;11:484.
[14] Huang Y, Kinloch AJ. J Mater Sci 1992;27:2763.
[15] Kody RS, Lesser AJ. J Mater Sci 1997;32:5637.
[16] Gurson AL. J Engng Mater Technol, Trans ASME 1977;99:2.
[17] Chen CC, Sauer JA. J Appl Polym Sci 1990;40:503–21.
[18] Sauer JA, Pae KD, Bhateja SK. J Macromol Phys 1973;B8:631.
[19] Crawford E, Lesser AJ. Polymer 2000;41:5865–70.
[20] Dompas D, Groeninckx G. Polymer 1994;35:4743.
[21] Bucknall CB, Karpodinis A, Zhang XC. J Mater Sci 1994:3377–83.
[22] Kachanov M. Int J Fract 1985;28:R11–9.
[23] Kachanov M, Montagut E. Engng Fract Mech 1986;25:625–36.
[24] Donald AM, Kramer EJ. J Mater Sci 1982;17:2351–8.
[25] Donald AM, Kramer EJ. J Appl Polym Sci 1982;27:3729–41.
[26] Sultan J, McGarry FJ. Polym Engng Sci 1973;13:29–34.
[27] Sternstein SS, Ongchin L. ACS Polym Prepr 1969;10:1117.
[28] Anderson TL. Fracture mechanics—fundamentals and applications. Boca Raton: CRC Press, 1995. Chapter 8, p. 439.
[29] Kachanov M, Laures JP. Int J Fract 1989;41:289–313.
[30] Dompas D, Groenickx G, Isogawa M, Hasegawa T, Kadokura M. Polymer 1994;35:4750–65.